



# Multiwavelength Observations of the Infrared Dust Bubble N75 and its Surroundings

Quan-Ling Cui<sup>1,2,3</sup>, Chuan-Peng Zhang<sup>1,4</sup> , and Jun-Jie Wang<sup>1</sup>

<sup>1</sup>National Astronomical Observatories, Chinese Academy of Sciences, Beijing 100101, China; [cpzhang@nao.cas.cn](mailto:cpzhang@nao.cas.cn)

<sup>2</sup>University of Chinese Academy of Sciences, Beijing 100049, China

<sup>3</sup>College of Science, Qiqihar University, Qiqihar 161006, China

<sup>4</sup>Guizhou Radio Astronomical Observatory, Guizhou University, Guiyang 550000, China

Received 2024 January 8; revised 2024 March 9; accepted 2024 March 18; published 2024 April 24

## Abstract

Infrared dust bubbles play an important role in the study of star formation and the evolution of the interstellar medium. In this work, we study the infrared dust bubble N75 and the infrared dark cloud G38.93 mainly using the tracers  $C^{18}O$ ,  $HCO^+$ ,  $HNC$  and  $N_2H^+$  observed by the 30 m IRAM telescope. We also study the targets using data from large-scale surveys: GLIMPSE, MIPS GAL, GRS, NRAO VLA Sky Survey and Bolocam Galactic Plane Survey. We found that the  $C^{18}O$  emission is morphologically similar to the Spitzer IRAC 8.0  $\mu m$  emission. The 1.1 mm cold dust emission of G38.93 shows an elongated structure from southwest to northeast. The ionized gas from G38.93 is surrounded by polycyclic aromatic hydrocarbon emission, which may be excited by radiation from G38.93. We found that the identified young stellar objects tend to cluster around G38.93 and are mostly in class II, with several class I cases distributed around N75, but no class II examples. We also found evidence of expanding feedback, which could have triggered star formation.

*Key words:* ISM: bubbles – infrared: ISM – galaxies: star formation

## 1. Introduction

Churchwell et al. (2006) detected and cataloged about 600 mid-infrared dust bubbles between longitudes  $-60^\circ$  and  $+60^\circ$ . Ionizing O- and/or B-type stars may play an important role in the formation of infrared (IR) dust bubbles (e.g., Zhang & Wang 2012, 2013; Zhang et al. 2013, 2016; Xu et al. 2014). These bubbles provide an important opportunity to study the interplay between the H II region and molecular clouds (e.g., Zhang & Wang 2012, 2013). Simpson et al. (2012) present a catalog of 5106 IR bubbles created by visual classification via the online citizen science website “The Milky Way Project.” Ultraviolet (UV) radiation from ionizing stars can heat dust and ionize gas, resulting in the formation of an expanding bubble shell (Watson et al. 2008). Massive star formation can be triggered by this process in the vicinity of shell clumps.

Some bubbles are associated with infrared dark clouds (IRDCs). The IRDCs harbor various evolutionary stages, provide good targets to study the initial conditions of massive star formation prior to cloud collapse and are important to understand the early evolution of massive star-forming clumps (Rathborne et al. 2006; Beuther et al. 2007; Henning et al. 2010). Therefore, IRDCs play an important role in the study of star formation and the evolution of the interstellar medium (ISM) (e.g., Rathborne et al. 2005; Pillai et al. 2006; Beuther & Sridharan 2007; Zhang et al. 2017a). Additionally, bubbles associated with IRDCs will provide an important

sample to study both triggered star formation and the early stage of high-mass star formation. The dense and cold nature of IRDCs may be more conducive to special chemical reactions than in other star formation regions (e.g., Zhang et al. 2017b, 2019, 2020). For example, CO, a commonly used tracer of dynamics in cold and dense clouds (Hernandez & Tan 2011), can be affected by depletion of the gas phase abundance due to freezing on dust grains (Hernandez et al. 2011). Due to the freeze-resistance of some N- or D-containing molecules, N- and D-bearing molecules such as  $N_2H^+$  are more suitable for tracing the dense and cold cores (e.g., Zhang et al. 2020).

G38.93-0.355 (hereafter G38.93) is an IRDC associated with an IR dust bubble N75 (Churchwell et al. 2006). The distance of G38.93 was measured to be 2.7 kpc (Zhang et al. 2014). Bubble N75 and IRDC G38.93 are good targets to study the triggered star formation and high-mass star formation. The masers, including  $H_2O$  masers (Forster & Caswell 1989, 1999), OH masers (Forster & Caswell 1989, 1999; Błaszczewicz & Kus 2004; Szymczak & Gérard 2004; Caswell et al. 2013), and class II  $CH_3OH$  masers (Błaszczewicz & Kus 2004; Szymczak & Gérard 2004), were detected in G38.93, suggesting massive star formation there. Xu et al. (2013) studied N75, N74 and their surrounding regions, however, they only used the optically thick CO as tracers to them. In this paper we use the new molecular spectra to perform a more detailed study of G38.93 to verify and complement the results of Xu et al. (2013).

In this paper we present a multiwavelength study in the bubble N75, mainly probing the ISM around N75 and searching for evidence of star formation. The observations and data reduction are described in Section 2; the results and data analysis are presented in Section 3; the discussion of the corresponding star formation is presented in Section 4. Section 5 is the conclusion.

## 2. Observation and Data

The adopted spectral data, covering the bubble N75 and the clump G38.93, are mainly from the IRAM 30 m and FCRAO 15 m telescopes. They are used to study the dense and cold structure. In addition, the dust and continuum data are from Spitzer and the NRAO VLA Sky Survey (NVSS) archival data for studying the IR and H II background. Details about observations and data are presented in the following sections.

### 2.1. IRAM 30 m Observations

The  $\text{HCO}^+$  (1–0),  $\text{HNC}$  (1–0),  $\text{N}_2\text{H}^+$  (1–0) and  $\text{C}^{18}\text{O}$  data observations were made in 2018 December with the IRAM 30 m telescope<sup>5</sup> on Pico Veleta, Spain. The half-power beamwidth was between  $29''.0$  and  $23''.5$ , the main beam efficiency ( $B_{\text{eff}}$ ) was between 81% and 78%, and the forward efficiency ( $F_{\text{eff}}$ ) of the IRAM 30 m telescope was between 95% and 94%. The relation between the main beam temperature ( $T_{\text{MB}}$ ) and the antenna temperature ( $T_{\text{A}}^*$ ) is  $T_{\text{MB}} = (F_{\text{eff}}/B_{\text{eff}}) \times T_{\text{A}}^*$ . The on-the-fly mapping mode was used to scan each source in two orthogonal directions to reduce striping on the maps. The data reduction software is GILDAS.<sup>6</sup>

### 2.2. $^{13}\text{CO}$ Data

The  $^{13}\text{CO}$  ( $J=1 \rightarrow 0$ ) data are from the Boston University-Five College Radio Astronomy Observatory Galactic Ring Survey<sup>7</sup> (GRS; Jackson et al. 2002). The data have a full width at half maximum (FWHM) of  $46''$  and a velocity resolution of  $0.21 \text{ km s}^{-1}$  at 110.2 GHz. The  $^{13}\text{CO}$  data will be used to map our target and calculate the physical parameters.

### 2.3. Dust and Continuum Data

The IR data are from the Spitzer GLIMPSE survey (Benjamin et al. 2003) and the MIPS GAL survey (Rieke et al. 2004). The NVSS is a 1.4 GHz continuum survey covering the entire sky north of  $-40^\circ$  decl. NVSS was used to trace the ionizing gas (Condon et al. 1998) with a noise of about  $0.45 \text{ mJy beam}^{-1}$ . We also used the 1.1 mm continuum data from the Bolocam Galactic Plane Survey (BGPS)<sup>8</sup>

(Aguirre et al. 2010) and the Bolocam 1.1 mm source catalog (Ginsburg et al. 2013) to trace the dense part of our target source. The effective FWHM of the 1.1 mm map is  $\sim 33''$ .

## 3. Results and Analysis

### 3.1. Dust Emission

Figure 1 displays the  $^{13}\text{CO}$  emission (white), 1.1 mm emission (cyan) and 1.4 GHz continuum emission (red) contours superimposed on the three-color image of  $4.5 \mu\text{m}$  (blue),  $8.0 \mu\text{m}$  (green) and  $24 \mu\text{m}$  (red). The Spitzer IRAC 8 m emission may originate from polycyclic aromatic hydrocarbons (PAHs), which are excited by the photodissociated region surrounding the H II region (Pomarès et al. 2009; Petriella et al. 2010). The  $8 \mu\text{m}$  emission is extended at G38.93. The H II region N74, located to the southeast of N75, shows a ring-like shape. The  $24 \mu\text{m}$  emission, originating from hot dust, appears to be inside the bubble of N75 and N74. The  $4.5 \mu\text{m}$  emission indicates the location of the brightest stars.

The 1.1 mm continuum emission is from cold dust. The cold dust emission of G38.93 shows an elongated structure from southwest to northeast. The structure of G38.93 is outlined by the 1.1 mm emission, which is comparable to the shape of the molecular emission contours in Figure 2. We used the NVSS 1.4 GHz continuum emission overlaid on the three-color map to trace the ionized gas in the H II region.

### 3.2. Integrated Intensity Maps

We draw the integrated intensity maps of G38.93 and N75 in Figure 2. The  $^{13}\text{CO}(J=1-0)$  can be used to trace the structure of the clump associated with the H II region. We find that the composition of CO velocity, ranging from 35 to  $42 \text{ km s}^{-1}$ , is related to these H II regions. We present an integrated intensity map of  $^{13}\text{CO}(J=1-0)$  in Figure 1, where two dense clumps, labeled with G38.93 and G38.95, can be clearly seen. Additionally, G38.93 is located at the northwest of N75, and has a compressed structure as seen from the CO distribution in Figure 1, suggesting a likely interaction between the N75 and G38.93.

We also find that the  $\text{HCO}^+$ ,  $\text{N}_2\text{H}^+$  and  $\text{HNC}$  emissions have similar morphologies to the 1.1 mm emission, while the  $\text{C}^{18}\text{O}$  emission is more extended. The  $\text{C}^{18}\text{O}$  emission and the  $8.0 \mu\text{m}$  emission are very similar in morphology. In Figure 2 we see that the  $\text{C}^{18}\text{O}$  emission is weaker in the center of N75. The  $\text{C}^{18}\text{O}$  emission may be optically thick at such condition.

### 3.3. Molecular Lines

From the BGPS 1.1 mm peak position of G38.93, we extracted individual  $\text{C}^{18}\text{O}$ ,  $\text{HCO}^+$ ,  $\text{HNC}$  and  $\text{N}_2\text{H}^+$  spectra. The average spectra of  $\text{C}^{18}\text{O}$ ,  $\text{HCO}^+$ ,  $\text{HNC}$  and  $\text{N}_2\text{H}^+$  are displayed in Figure 3. These spectra show that the main

<sup>5</sup> IRAM is supported by INSU/CNRS (France), MPG (Germany) and IGN (Spain).

<sup>6</sup> <http://www.iram.fr/IRAMFR/GILDAS/>

<sup>7</sup> <http://third.ucllnl.org/cgi-bin/gpscutoff>

<sup>8</sup> <http://irsa.ipac.caltech.edu/data/BOLOCAMGPS/>

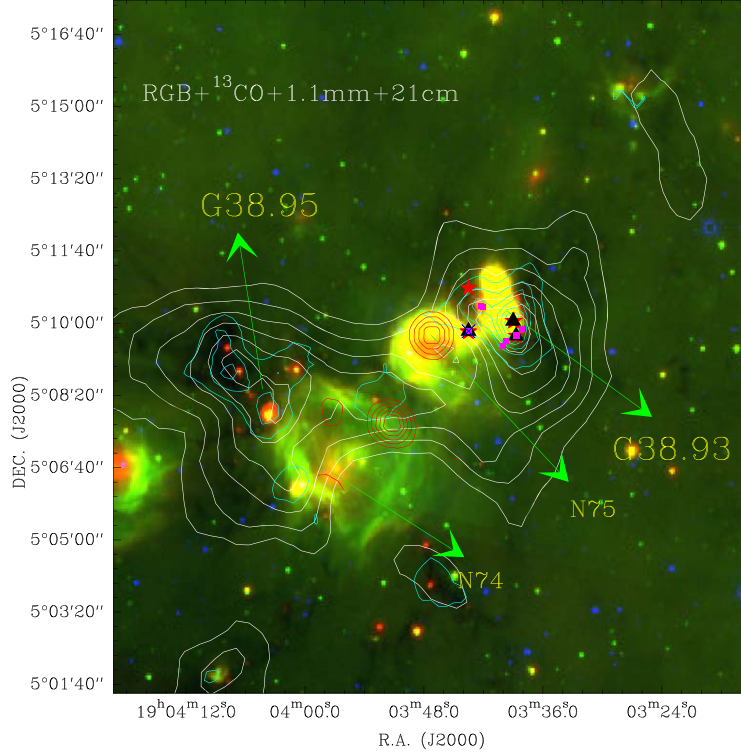


**Figure 1.** Three-color image toward H II region N75 and its surroundings with blue, green and red corresponding to  $4.5 \mu\text{m}$  (blue; Benjamin et al. 2003) and MIPS GAL  $8.0 \mu\text{m}$  (green; Benjamin et al. 2003) and MIPS GAL  $24 \mu\text{m}$  (red; Carey et al. 2009), respectively. BGPS  $1.1 \text{ mm}$  emission is shown in blue contours,  $^{13}\text{CO}$  emission is in white contours and the NVSS  $1.4 \text{ GHz}$  radio continuum emission is in red contours. The white and blue contour levels are 10%–100% of peak value by 10%. The symbols “■,” “▲,” “★” and “×” mark the locations of  $\text{CH}_3\text{OH}$  class II maser,  $\text{CH}_3\text{OH}$  class I masers,  $\text{H}_2\text{O}$  masers, and IRAS sources, respectively.

location of the velocity components is in the range of  $33\text{--}45 \text{ km s}^{-1}$ . We apply Gaussian fits to the spectra of  $\text{C}^{18}\text{O}$ ,  $\text{HCO}^+$ ,  $\text{HNC}$  and  $\text{N}_2\text{H}^+$ . The fitted results are summarized in Table 1. Then we derive a system velocity of  $\sim 38.98 \text{ km s}^{-1}$  using the  $\text{C}^{18}\text{O}$  line for clump G38.93.

### 3.4. Velocity Distribution

In Figure 4, we show the channel maps of  $\text{C}^{18}\text{O}(1\text{--}0)$  to examine the detailed velocity distribution in the clump. We found that the system velocity of the bubble N75 is  $\sim 40.5 \text{ km s}^{-1}$ . Figure 5 presents the channel maps of the  $\text{HCO}^+$  line. We can see that the  $8.0 \mu\text{m}$  grayscale shows the position and size of N74, N75 and G38.93. The  $\text{HCO}^+$  emission extends over a velocity range of  $34 < V_{\text{LSR}} < 42 \text{ km s}^{-1}$ , while  $\text{C}^{18}\text{O}$  emission extends over a velocity range of  $37.5 < V_{\text{LSR}} < 41.5 \text{ km s}^{-1}$ . Based on the above velocity range, we make the position–velocity (PV) diagram of  $\text{HCO}^+$  as displayed in Figure 8. Considering the PV diagram, we make the integral intensity maps of G38.93 as depicted in Figure 6. The blue contours indicate the blueshift velocity components and the red contours correspond to the redshift velocity components, suggesting the existence of outflow.

**Table 1**  
Spectral Parameters of Molecular Cores at the G38.93

Name	Area ( $\text{K km s}^{-1}$ )	Position ( $\text{km s}^{-1}$ )	Width ( $\text{km s}^{-1}$ )	Intensity (K)
$\text{C}^{18}\text{O}$	2.729(0.056)	38.980(0.032)	3.031(0.069)	0.845
$\text{HCO}^+$	4.546(0.022)	40.659(0.007)	2.875(0.016)	1.485
$\text{HNC}$	1.989(0.022)	40.610(0.012)	2.313(0.033)	0.807
$\text{N}_2\text{H}^+$	1.851(0.017)	38.550(0.157)	3.850(0.157)	0.452
$^{13}\text{CO}$	13.884(0.381)	40.339(0.047)	3.47(0.108)	3.748

### 3.5. Dust Temperature and Density

In order to study the effects of the H II regions on G38.93, it is crucial to calculate the temperature and density. Herschel observations covering a wavelength range ( $70\text{--}500 \mu\text{m}$ ) can be used to construct the ( $N_{\text{H}_2}$ ) column density and dust temperature maps at  $160$ ,  $250$ ,  $350$  and  $500 \mu\text{m}$ . The reason we exclude  $70 \mu\text{m}$  is that  $70 \mu\text{m}$  emission traces hotter components heated by UV emission. Using the Getsources algorithm (Men’shchikov et al. 2010, 2012; Men’shchikov 2013), we created the column density and dust temperature maps of G38.93 by fitting the spectral energy distributions (SEDs) on a pixel-by-pixel basis (Palmeirim et al. 2013).

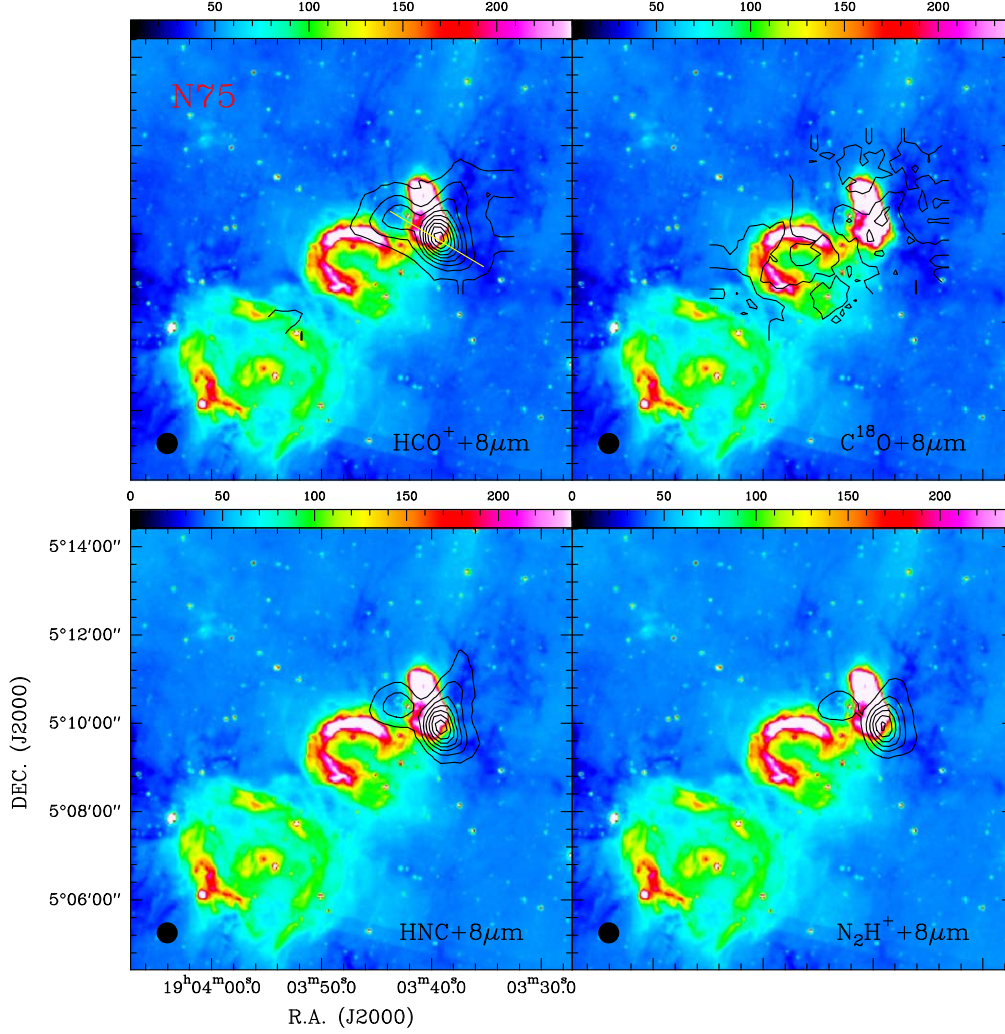


**Figure 2.** Integrated intensity maps of  $\text{HCO}^+$ ,  $\text{C}^{18}\text{O}$ ,  $\text{HNC}$  and  $\text{N}_2\text{H}^+$  lines on the Spitzer  $8\mu\text{m}$  emission. The integrated velocity intervals are  $33\text{--}45\text{ km s}^{-1}$ . The  $\text{HCO}^+$  contour levels start at  $3\sigma$  in steps of  $3\sigma$  ( $\sigma = 0.1\text{ K km s}^{-1}$ ). The beam size of each subfigure is indicated at the bottom-left contour. The straight line in the  $\text{HCO}^+$  subfigure shows the cutting direction of the PV diagram in Figure 8. The unit of each color bar is in  $\text{MJy sr}^{-1}$ .

Figure 7 shows the  $T_{\text{dust}}$  and  $N_{\text{H}_2}$  maps. We found that the  $T_{\text{dust}}$  distribution ranges from 10 to 30 K, and the column density is about  $10^{22}\text{ cm}^{-2}$  with a maximum column density of about  $9.73 \times 10^{22}\text{ cm}^{-2}$ . The temperature reaches minimum at the column density peak position of G38.93. Furthermore, the mean dust temperature is about 15.6 K, suggesting a relatively cold condition in this star formation region.

### 3.6. Excitation Temperature, Column Density and Mass for G38.93

Using the molecular lines, we calculate the physical parameters  $T_{\text{ex}}$ ,  $N_{\text{H}_2}$ ,  $n(\text{H}_2)$  and  $M_{\text{LTE}}$  of G38.93 with a kinematic distance of 2.70 kpc (Roman-Duval et al. 2009). Assuming local thermodynamic equilibrium (LTE), we use the relatively optically thin  $^{13}\text{CO}(J=1-0)$  emission to determine

the column densities and mass of the G38.93 clump by applying the following equation (Garden et al. 1991)

$$N(^{13}\text{CO}) = 4.57 \times 10^{13} \frac{(T_{\text{ex}} + 0.89)}{\exp(-5.29/T_{\text{ex}})} \int T_{\text{mb}} dv (\text{cm}^{-2}), \quad (1)$$

where  $T_{\text{mb}}$  is the corrected main-beam temperature of  $^{13}\text{CO}$ , and  $T_{\text{ex}}$  is the excitation temperature in K.  $T_{\text{ex}}$  can be calculated by the following equation (Garden et al. 1991)

$$T_{\text{ex}} = \frac{5.29}{\ln[1 + 5.29/(T_{\text{mb}}(^{13}\text{CO}) + 0.89)]}. \quad (2)$$

The  $\text{H}_2$  column density is calculated with the following equation (Frerking et al. 1982)

$$N(\text{H}_2)/N(^{13}\text{CO}) = 5 \times 10^5. \quad (3)$$

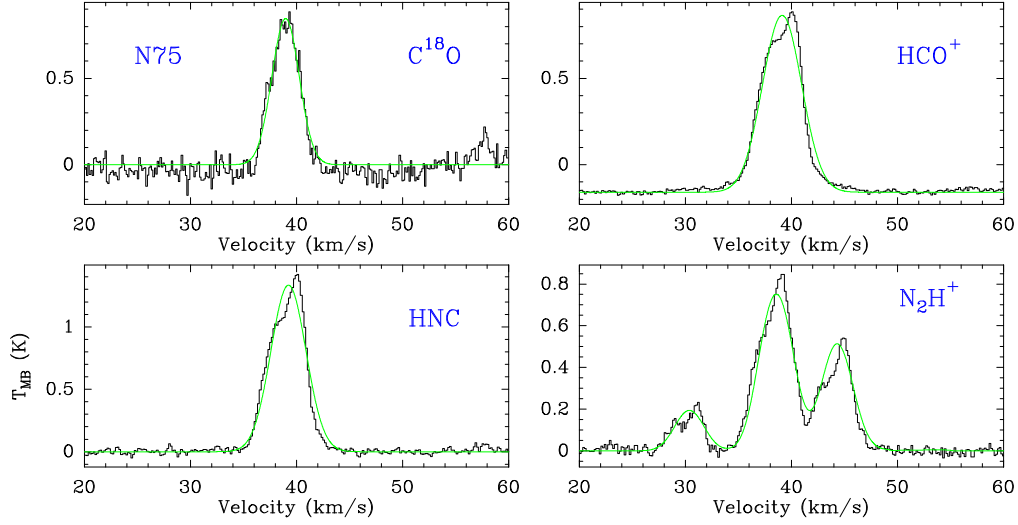


**Figure 3.** The spectra of  $C^{18}O$ , HNC,  $N_2H^+$  and  $HCO^+$  lines at the clump G38.93. The green curves show the Gaussian fitting results.

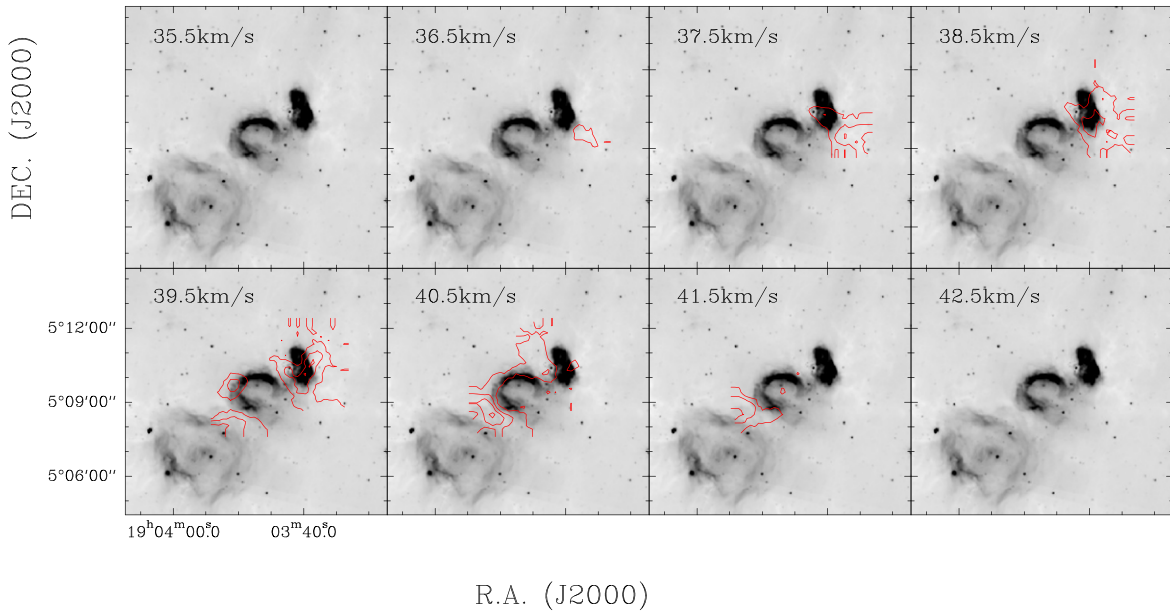


**Figure 4.** Channel maps of the  $C^{18}O$  line over the velocity interval  $35.5\text{--}42.5\text{ km s}^{-1}$ . The integrated velocity interval of each image is  $1\text{ km s}^{-1}$ . The central velocities are shown in each image.

Then the mean volume densities of the  $H_2$  molecule are

$$n(H_2) = N(H_2)/2R. \quad (4)$$

Based on the assumption of LTE and spherical geometry, the masses of the clouds are calculated as

$$M_{\text{LTE}} = \mu m_H n(H_2) \times \left( \frac{4}{3} \pi R^3 \right), \quad (5)$$

where  $m_H$  is the mass of a hydrogen atom and  $\mu = 2.8$  is the mean molecular weight considering the contributions of  $H_e$  and other heavy elements to the total mass.

Finally, we derived the column density of the clump G38.93 with  $N(H_2) = 5.34 \times 10^{21}\text{ cm}^{-2}$ . Other corresponding parameters are  $n(H_2) = 1.16 \times 10^3\text{ cm}^{-3}$ ,  $R_{\text{min}} = 4'.2$ ,  $R = 3.055\text{ pc}$ ,  $D = 2.5\text{ kpc}$ ,  $T_{\text{ex}} = 6.953\text{ K}$ ,  $N(^{13}CO) = 1.068 \times 10^{16}\text{ cm}^{-2}$  and  $M_{\text{LTE}} = 8 \times 10^4 M_{\odot}$ .

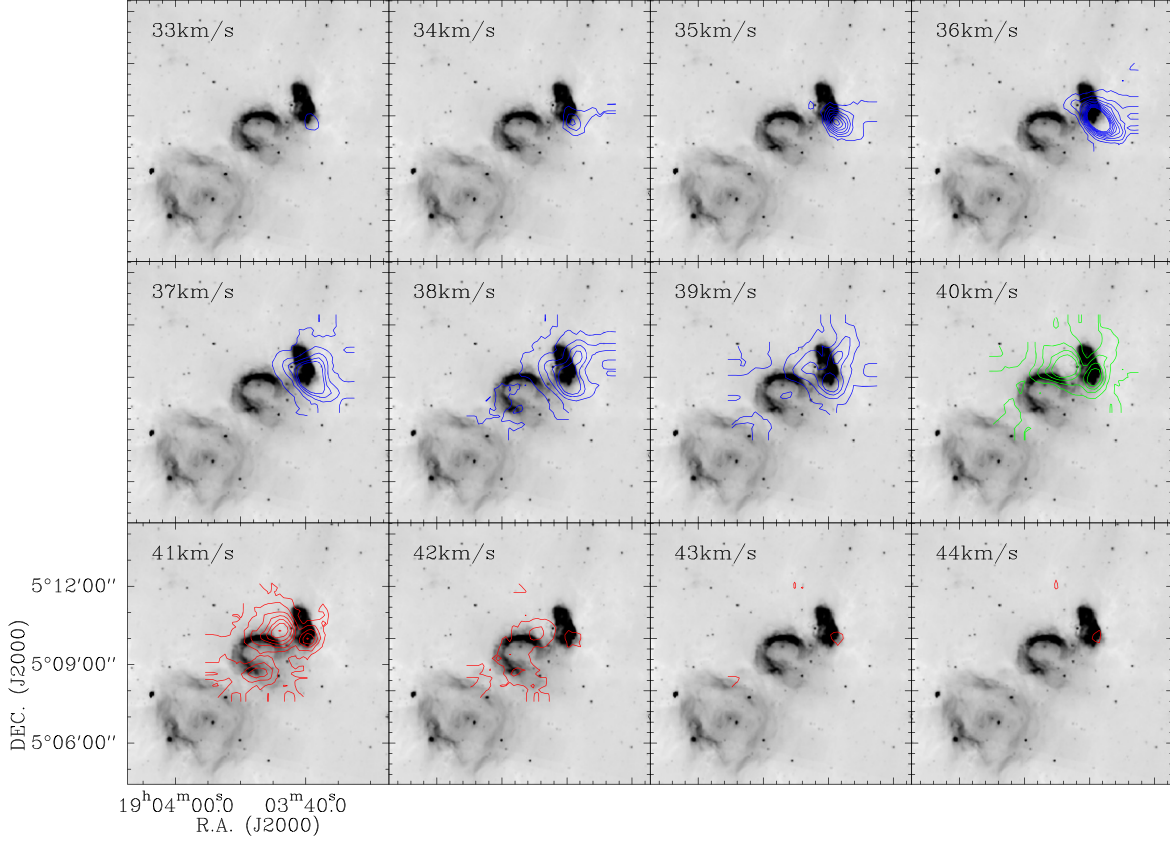


**Figure 5.** The channel maps of the  $\text{HCO}^+$  line over the velocity interval of 33–44  $\text{km s}^{-1}$ . The integrated velocity interval of each slice is 1  $\text{km s}^{-1}$ , and central velocities are given in each image. The blue contours range from 33 to 39  $\text{km s}^{-1}$  and the red contours range from 40 to 44  $\text{km s}^{-1}$ .

### 3.7. Outflow

The PV diagram for G38.93 is visualized in Figure 8. The cutting direction passing through the selected dense core positions is indicated by the yellow line in the  $\text{HCO}^+$  subfigure of Figure 2. The dense cores are the backbone of the G38.93 clump and allow us to study its dynamical state. The PV plot shows a clear velocity gradient relative to the system velocity of 39  $\text{km s}^{-1}$ . The broad and extended line wings of the  $\text{HCO}^+$  in Figure 3 represent the blueshifted and redshifted velocity components respectively. The PV diagram in Figure 8 provides additional evidence for the outflow (Smith et al. 1997; Beuther et al. 2004).

We selected the integrated area of the wings and determined the outflow intensities of the red and blue lobes according to the PV plots and channel maps. The contours of the integrated intensities of the  $\text{HCO}^+$  line wing identified a molecular outflow (Figure 6). The dynamic timescale of the outflow is calculated using the equation  $t_{\text{out}} = 9.78 \times 10^5 R/V$  (yr), where  $R$  in pc is the outflow size and  $V$  in  $\text{km s}^{-1}$  is the maximum flow velocity relative to the cloud system velocity. The mean dynamic timescale of the outflow is  $5.1 \times 10^5$  yr.

### 3.8. Expansion Age of the Bubble N75

Using the 1.4 GHz radio continuum emission, the ionizing luminosity  $N_{\text{Ly}}$  was computed via Mezger et al. (1974) with

$$N_{\text{Ly}} = 4.76 \times 10^{48} \left( \frac{\nu}{\text{GHz}} \right)^{0.1} \left( \frac{T_e}{\text{K}} \right)^{-0.45} \left( \frac{S_\nu}{\text{Jy}} \right) \left( \frac{D}{\text{kpc}} \right)^2 \text{ s}^{-1}. \quad (6)$$

Here we adopted an effective electron temperature of  $10^4$  K, the distance 2.7 kpc and  $S_\nu = 23.7$  mJy. We derived  $N_{\text{Ly}} = 2.14 \times 10^{46} \text{ s}^{-1}$ . Assuming the H II region is expanding into a homogeneous medium, the dynamical age was estimated by the method of Dyson & Williams (1980)

$$t_{\text{H II}} = 7.2 \times 10^4 \left( \frac{R_{\text{H II}}}{\text{pc}} \right)^{4/3} \left( \frac{N_{\text{Ly}}}{10^{49} \text{ s}^{-1}} \right)^{-0.25} \left( \frac{n_i}{10^3 \text{ cm}^{-3}} \right)^{-0.5} \text{ yr}. \quad (7)$$

The age of the H II region G38.93 is  $1.38 \times 10^6$  yr.

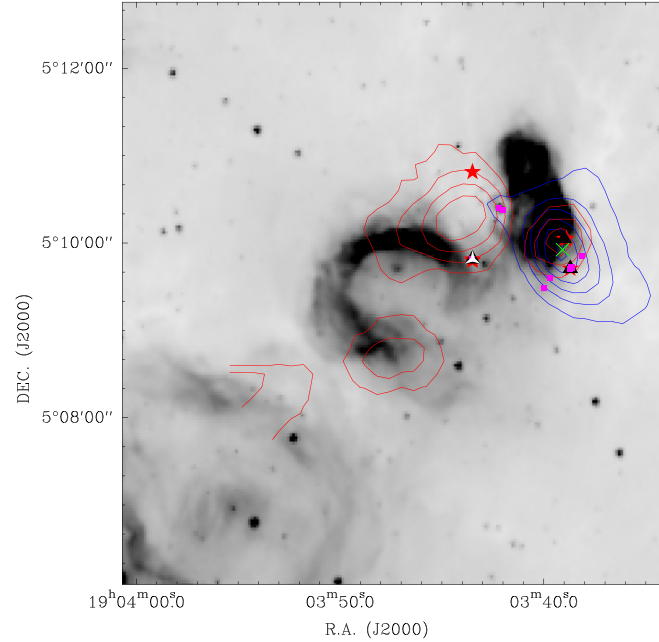


**Figure 6.** Integrated intensity map of the  $\text{HCO}^+$  outflow (red and blue contours) superimposed on the Spitzer  $8\ \mu\text{m}$  emission. The red and blue contours are 30%, ..., 100% of the peak. The red squares and triangle represent the IRAS sources and the Class II methanol maser (Deharveng et al. 2010) respectively. The beam size is given in the lower left corner. The symbols “ $\diamond$ ,” “ $\triangle$ ,” “ $\star$ ,” “ $\blacksquare$ ,” “ $\blacktriangle$ ” and “ $\times$ ” indicate the location of an OH maser, IRAS,  $\text{CH}_3\text{OH}$  masers,  $\text{H}_2\text{O}$  masers and the peak positions, respectively. The green cross marks a BGPS source.

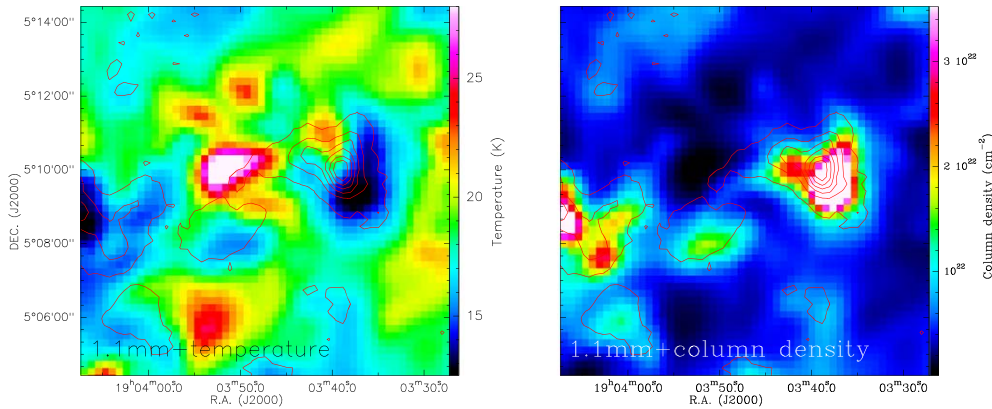


**Figure 7.** Left panel: the BGPS 1.1 mm continuum emission (red contours) overlaid on the Herschel temperature map. Right panel: the BGPS 1.1 mm continuum emission (red contours) superimposed on the Herschel column density. Both maps were constructed using the SED pixel-by-pixel fit.

## 4. Discussion

### 4.1. Star Formation Activity

The molecular outflows (see Figure 6) and masers such as  $\text{H}_2\text{O}$ , OH, and Class II  $\text{CH}_3\text{OH}$  (Caswell et al. 1995) were detected surrounding the bubble N75 and G38.93. This indicates that such a star formation system is an active star formation region. Furthermore, we also found many young stellar objects (YSOs) associated with this star

formation system, so that we could derive their spatial distribution, ages, and masses. Based on the criteria of Allen et al. (2004), we selected near-infrared sources with 3.6, 4.5, 5.8, and  $8.0\ \mu\text{m}$  emission in our survey region from the GLIMPSE point source catalog. Figure 9 shows the [5.8]–[8.0] versus [3.6]–[4.5] color–color diagram. Only sources detectable in four Spitzer IRAC bands were considered. In Figure 9, class I YSOs are protostars with circumstellar envelopes, class II YSOs are disk-dominated objects and

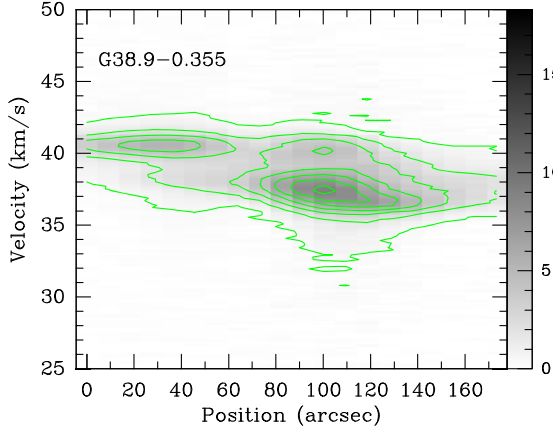


**Figure 8.** PV diagram of  $\text{HCO}^+$  along the straight line of the clump G38.93 in Figure 2. The contour levels start from  $5\sigma$  to the peak integrated intensity of  $5\sigma$  ( $\sigma = 0.146$  K). The gray bar represents the intensity in Kelvin.

class III cases are main sequence or giant stars. From Figure 10, YSOs tend to cluster around G38.93 and mostly in class II, with several class I instances distributed around N75, but no class II cases. The ages of class I YSOs are  $\sim 10^5$  yr, while the lifetimes of class II YSOs are  $\sim 10^6$  yr (Andre & Montmerle 1994).

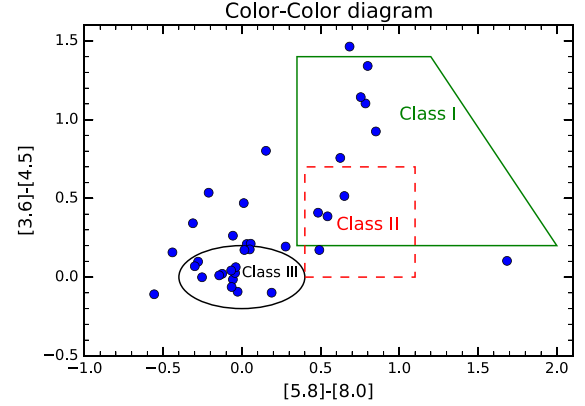


**Figure 9.** GLIMPSE color-color diagram  $[5.8]-[8.0]$  vs.  $[3.6]-[4.5]$  for sources in and around G38.93. Class I, II and III sources are indicated with different color areas. The classification as Class I, II, or III suggests the stellar evolutionary stage as defined by Allen et al. (2004).

#### 4.2. Triggered Star Formation

Figure 10 shows an RGB image with  $4.5 \mu\text{m}$ ,  $8 \mu\text{m}$  and  $24 \mu\text{m}$  in blue, green, and red, respectively. The positions of the candidate YSOs are shown in Figure 10, where Class I and Class II YSOs are indicated by black and red dots,

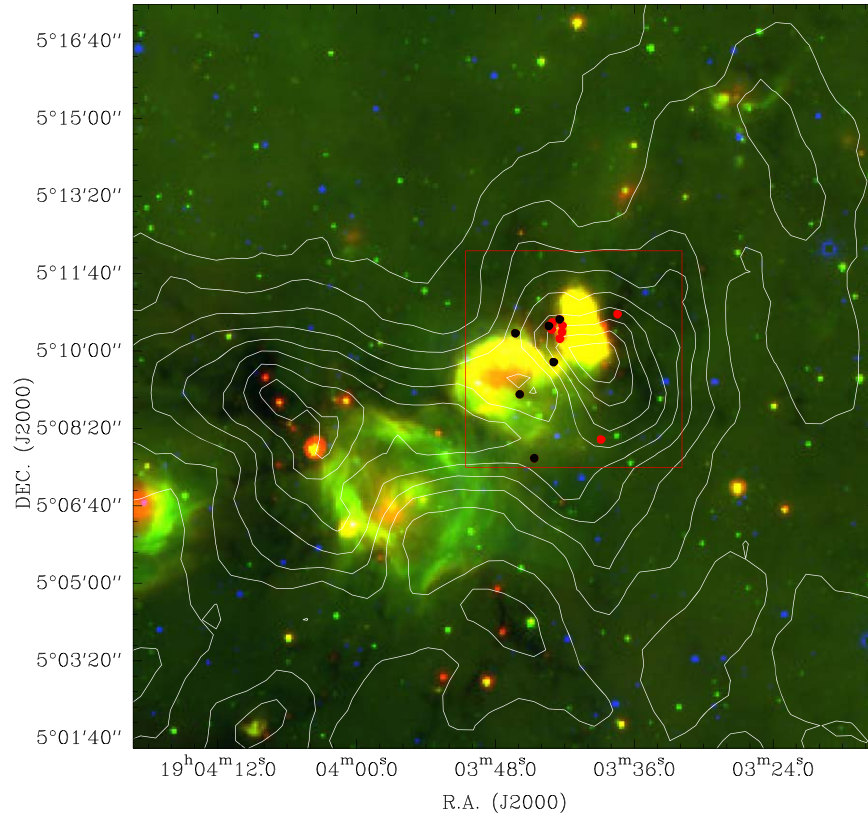


**Figure 10.** Three-color image with IRAC  $4.5 \mu\text{m}$ ,  $8 \mu\text{m}$  and MIPS  $24 \mu\text{m}$  in blue, green, and red respectively. Class I and II YSOs are marked with black and red dots respectively. White outlines are  $^{13}\text{CO}$  emission. The square indicates the area for the identified YSOs.

respectively. The YSOs are mainly located in the compressed regions between bubble N75 and G38.93, suggesting that expanding feedback could have triggered star formation. Four Class I stars are located on the compact shell of bubble N75, which may indicate triggered star formation. The age of N75 is larger than that of those Class I stars, suggesting that there is enough time for this trigger process. Class II stars are concentrated at the east of G38.93 with strong  $8\ \mu\text{m}$  emission. The  $8\ \mu\text{m}$  emission distribution has a cocoon-like structure, which could be a compact H II region ionized by massive star formation. It is probably that the expansion of such a compact H II region has triggered the formation of class II stars, the masers and the outflows. We note that only a few YSOs are consistent with the bright bubble edges. It is possible that some YSOs are simply hidden in the high IR background, and the YSOs are mainly located in the compressed regions between the bubble N75 and G38.93. This may suggest that expanding feedback could have triggered star formation.

## 5. Conclusions

In this work, we studied bubble N75 with  $\text{C}^{18}\text{O}$ ,  $\text{HCO}^+$ , HNC, and  $\text{N}_2\text{H}^+$ , and performed a multiwavelength study around G38.93. We found morphologically the  $\text{C}^{18}\text{O}$  emission correlates well with the Spitzer IRAC  $8.0\ \mu\text{m}$  emission. The east of G38.93 shows an arc-like shape, with a small area of higher PAH emission in the center. The  $1.1\ \text{mm}$  emission, tracing the cold dust, outlines the shape of G38.93, which is similar to the shape of the molecular emission. The cold dust emission of G38.93 exhibits an elongated structure from southwest to northeast. The  $1.4\ \text{GHz}$  continuum emission shows the ionized gas in G38.93. The ionized gas from G39.93 is surrounded by the PAH emission, which may be excited by radiation from G38.93. We found that the identified YSOs tend to cluster around G38.93 and mostly in class II, with several class I cases distributed around N75, but no class II examples. We also found evidence of expanding feedback, which could have triggered star formation.

## Acknowledgments

This work is supported by the National Key R&D Program of China (No. 2022YFA1602901), the local Science and Technology innovation projects of the central government (No. XZ202301YD0037C), and the National Natural Science Foundation of China (No. 11933011). We also wish to thank the anonymous referee for comments that improved the clarity of the paper.

## ORCID iDs

Chuan-Peng Zhang  <https://orcid.org/0000-0002-4428-3183>

## References

- Aguirre, J. E., Ginsburg, A. G., Dunham, M. K., et al. 2010, *ApJS*, **192**, 4  
 Allen, L. E., Calvet, N., D'Alessio, P., et al. 2004, *ApJS*, **154**, 363  
 Andre, P., & Montmerle, T. 1994, *ApJ*, **420**, 837  
 Benjamin, R. A., Churchwell, E., Babler, B. L., et al. 2003, *PASP*, **115**, 953  
 Beuther, H., Churchwell, E. B., McKee, C. F., & Tan, J. C. 2007, in *Protostars and Planets V*, ed. B. Reipurth, D. Jewitt, & K. Keil (Tucson, AZ: Univ. Arizona Press), 165  
 Beuther, H., Schilke, P., & Gueth, F. 2004, *ApJ*, **608**, 330  
 Beuther, H., & Sridharan, T. 2007, *ApJ*, **668**, 348  
 Błazkiewicz, L., & Kus, A. 2004, *A&A*, **413**, 233  
 Carey, S., Noriega-Crespo, A., Mizuno, D., et al. 2009, *PASP*, **121**, 76  
 Caswell, J., Green, J., & Phillips, C. 2013, *MNRAS*, **431**, 1180  
 Caswell, J., Vaile, R., Ellingsen, S., Whiteoak, J., & Norris, R. 1995, *MNRAS*, **272**, 96  
 Churchwell, E., Povich, M., Allen, D., et al. 2006, *ApJ*, **649**, 759  
 Condon, J. J., Cotton, W., Greisen, E., et al. 1998, *AJ*, **115**, 1693  
 Deharveng, L., Schuller, F., Anderson, L., et al. 2010, *A&A*, **523**, A6  
 Dyson, J. E., & Williams, D. A. 1980, *Physics of the Interstellar Medium* (Bristol: IOPP)  
 Forster, J., & Caswell, J. 1989, *A&A*, **213**, 339  
 Forster, J., & Caswell, J. 1999, *A&AS*, **137**, 43  
 Frerking, M., Langer, W., & Wilson, R. 1982, *ApJ*, **262**, 590  
 Garden, R., Hayashi, M., Gatley, I., Hasegawa, T., & Kaifu, N. 1991, *ApJ*, **374**, 540  
 Ginsburg, A., Glenn, J., Rosolowsky, E., et al. 2013, *ApJS*, **208**, 14  
 Henning, T., Linz, H., Krause, O., et al. 2010, *A&A*, **518**, L95  
 Hernandez, A. K., & Tan, J. C. 2011, *ApJ*, **730**, 44  
 Hernandez, A. K., Tan, J. C., Caselli, P., et al. 2011, *ApJ*, **738**, 11  
 Jackson, J. M., Bania, T., Simon, R., et al. 2002, *ApJL*, **566**, L81  
 Men'shchikov, A. 2013, *A&A*, **560**, A63  
 Men'shchikov, A., André, P., Didelon, P., et al. 2010, *A&A*, **518**, L103  
 Men'shchikov, A., André, P., Didelon, P., et al. 2012, *A&A*, **542**, A81  
 Mezger, P. G., Smith, L. F., & Churchwell, E. 1974, *A&A*, **32**, 269  
 Palmeirim, P. a., André, P., Kirk, J., et al. 2013, *A&A*, **550**, A38  
 Petriella, A., Paron, S., & Giacani, E. 2010, *A&A*, **513**, A44  
 Pillai, T., Wyrowski, F., Carey, S. J., & Menten, K. M. 2006, *A&A*, **450**, 569  
 Pomarès, M., Zavagno, A., Deharveng, L., et al. 2009, *A&A*, **494**, 987  
 Rathborne, J. M., Jackson, J., Chambers, E., et al. 2005, *ApJL*, **630**, L181  
 Rathborne, J. M., Jackson, J., & Simon, R. 2006, *ApJ*, **641**, 389  
 Rieke, G., Young, E., Engelbracht, C., et al. 2004, *ApJS*, **154**, 25  
 Roman-Duval, J., Jackson, J. M., Heyer, M., et al. 2009, *ApJ*, **699**, 1153  
 Simpson, R. J., Povich, M. S., Kendrew, S., et al. 2012, *MNRAS*, **424**, 2442  
 Smith, M. D., Suttner, G., & Yorke, H. W. 1997, *A&A*, **323**, 223  
 Szymczak, M., & Gérard, E. 2004, *A&A*, **414**, 235  
 Watson, C., Povich, M., Churchwell, E., et al. 2008, *ApJ*, **681**, 1341  
 Xu, J.-L., Wang, J.-J., & Liu, X.-L. 2013, *A&A*, **559**, A113  
 Xu, J.-L., Wang, J.-J., Ning, C.-C., & Zhang, C.-P. 2014, *RAA*, **14**, 47  
 Zhang, B., Moscadelli, L., Sato, M., et al. 2014, *ApJ*, **781**, 89  
 Zhang, C.-P., Csengeri, T., Wyrowski, F., et al. 2019, *A&A*, **627**, A85  
 Zhang, C.-P., Li, G.-X., Pillai, T., et al. 2020, *A&A*, **638**, A105  
 Zhang, C.-P., Li, G.-X., Wyrowski, F., et al. 2016, *A&A*, **585**, A117  
 Zhang, C. P., & Wang, J. J. 2012, *A&A*, **544**, A11  
 Zhang, C.-P., & Wang, J.-J. 2013, *RAA*, **13**, 47  
 Zhang, C.-P., Wang, J.-J., & Xu, J.-L. 2013, *A&A*, **550**, A117  
 Zhang, C.-P., Yuan, J.-H., Li, G.-X., Zhou, J.-J., & Wang, J.-J. 2017a, *A&A*, **598**, A76  
 Zhang, C.-P., Yuan, J.-H., Xu, J.-L., et al. 2017b, *RAA*, **17**, 057